Singlet-catalyzed electroweak phase transitions in the 100 TeV frontier

Ashutosh V. Kotwal, Michael J. Ramsey-Musolf, Jose Miguel No, and Peter Winslow

Singlet-Catalyzed Electroweak Phase Transitions in the 100 TeV Frontier

Ashutosh V. Kotwal,[1, 2, *] Michael J. Ramsey-Musolf,[3, 4, †] Jose Miguel No,[5, ‡] and Peter Winslow[3, §]

[1]*Fermi National Accelerator Laboratory, Batavia, IL 60510, USA*
[2]*Department of Physics, Duke University, Durham, NC 27708, USA*
[3]*Physics Department, University of Massachusetts Amherst, Amherst, MA 01003, USA*
[4]*Kellogg Radiation Laboratory, California Institute of Technology, Pasadena, CA 91125, USA*
[5]*Department of Physics and Astronomy, University of Sussex, BN1 9QH Brighton, UK*

We study the prospects for probing a gauge singlet scalar-driven strong first order electroweak phase transition with a future proton-proton collider in the 100 TeV range. Singlet-Higgs mixing enables resonantly-enhanced di-Higgs production, potentially aiding discovery prospects. We perform Monte Carlo scans of the parameter space to identify regions associated with a strong first-order electroweak phase transition, analyze the corresponding di-Higgs signal, and select a set of benchmark points that span the range of di-Higgs signal strengths. For the $b\bar{b}\gamma\gamma$ and 4τ final states, we investigate discovery prospects for each benchmark point for the high luminosity phase of the Large Hadron Collider and for a future pp collider with $\sqrt{s} = 50$, 100, or 200 TeV. We find that any of these future collider scenarios could significantly extend the reach beyond that of the high luminosity LHC, and that with $\sqrt{s} = 100$ TeV (200 TeV) and 30 ab^{-1}, the full region of parameter space favorable to strong first order electroweak phase transitions is almost fully (fully) discoverable.

I. INTRODUCTION

With the discovery of a Higgs-like boson [1, 2] the detailed nature of electroweak symmetry-breaking (EWSB) has come into sharp focus. While subsequent analyses have shown that the interactions of this new particle closely resemble those expected for the Standard Model (SM) Higgs boson, the possibility that it resides within an larger scalar sector remains quite open. Theoretically, an extended scalar sector is motivated by a number of considerations, including solutions to the hierarchy problem, mechanisms for neutrino mass generation, and dark matter models.

One of most compelling reasons to postulate an extended scalar sector is to explain the origin of the baryon asymmetry of the Universe (BAU):

$$Y_B = \frac{n_B}{s} = (8.59 \pm 0.11) \times 10^{-11} \quad \text{(Planck) [3]} \quad (1)$$

where n_B (s) is the baryon number (entropy) density. It is well known that the SM cannot accommodate the observed BAU, as it fails to provide for both the required CP-violation and the necessary out-of-equilibrium conditions in the early Universe [4]. While there exist a wide array of scenarios that address these SM shortcomings, one of the most theoretically attractive and experimentally testable is electroweak baryogenesis (for a recent review see, e.g. [5]), wherein Y_B is created during the electroweak phase transition (EWPT). Successful electroweak baryogenesis requires that the EWPT be strongly first order. Monte Carlo lattice simulations indicate that EWSB in the SM occurs through a cross-over transition [6–10] for a Higgs boson heavier than $70 - 80$ GeV, thereby precluding electroweak baryogenesis. However, if new bosonic states are present at the electroweak scale, the extra interactions can induce the desired strong first-order electroweak phase transition (SFOEWPT).

In this study, we investigate the possibility that a next generation proton-proton collider may discover one of the simplest realizations of this possibility: the extension of the SM scalar sector with a single, real gauge singlet, referred to henceforth as the "xSM". As outlined in Ref. [11], this simple scenario may both accommodate a SFOEWPT and provide for a rich collider phenomenology that may be used to probe it. In general, the xSM yields two mixed doublet-singlet scalars, h_1 and h_2, that are "SM-like" "singlet-like", respectively. Among the possible signatures are exotic h_1 decays, modifications of the Higgs signal strengths, and resonant production of h_1 pairs. Subsequent work also highlighted the correlation between the SFOEWPT and modifications of the h_1 trilinear self-coupling [12] and, for a $\mathbb{Z}_2$-symmetric version of the xSM, production of pairs of singlet scalars that do not mix with the Higgs boson [13][1].

Here, we concentrate on resonant di-Higgs production. It is well known that the xSM can generate a SFOEWPT in regions of parameter space that parametrically enhance resonant di-Higgs production *via* large $h_2 h_1 h_1$ trilinear couplings [11, 14, 15]. Previous work indicates that for relatively light h_2, discovery in the $b\bar{b}\tau^+\tau^-$ channel may be possible at the LHC with $\sqrt{s} = 14$ TeV and 100 fb^{-1} of integrated luminosity[15]. In this work, we carry out a more comprehensive study, focusing on the $b\bar{b}\gamma\gamma$ and 4τ states. We find that:

---

*Electronic address: `ashutosh.kotwal@duke.edu`
†Electronic address: `mjrm@physics.umass.edu`
‡Electronic address: `J.M.No@sussex.ac.uk`
§Electronic address: `pwinslow@physics.umass.edu`

---

[1] Probing the SFOEWPT in a xSM scenario with an exact $\mathbb{Z}_2$ symmetry is challenging but may be possible via S pair production in vector boson fusion through an off-shell Higgs boson [13].

- A future pp collider with $\sqrt{s} = 100$ TeV (200) could enable discovery of the xSM in nearly all (all) of the SFOEWPT-viable parameter space with 30 ab^{-1} of integrated luminosity.

- A future pp collider with $\sqrt{s} = 50$ TeV would significantly extend the reach of the high-luminosity phase of the Large Hadron Collider (HL-LHC), but would not provide the comprehensive coverage afforded by a 100 TeV collider.

- A SFOEWPT could occur in the xSM even if the HL-LHC and a future e^+e^- collider were to constrain the singlet-doublet mixing angle $|\theta| \lesssim 0.08$. In this case, discovery with a 100 TeV pp collider would still remain possible.

In arriving at these findings, we first determine the xSM parameter space favorable to a SFOEWPT using Monte Carlo (MC) methods, focusing on the region $m_2 > 2m_1$ where resonant di-Higgs production is kinematically allowed (for an analysis of the region $m_2 < 2m_1$, see [16]). We then investigate the discovery prospects for resonant di-Higgs production at future pp collider scenarios by identifying a set of 22 benchmark parameter points that span both the SFOEWPT-viable parameter space and the range of associated di-Higgs signal strengths. We focus on the $b\bar{b}\gamma\gamma$ and 4τ final states, chosen for their clean signatures despite their relatively small cross sections. We analyze the reach of both the HL-LHC and three different beam energies for a future pp collider ($\sqrt{s} = 50$, 100, and 200 TeV) as well as several total integrated luminosity goals.

We consider detectors with similar performance as the LHC detectors, using this scenario to set the scale for what could be achievable at a next-generation pp collider. We find that both final states studied here provide for comparable sensitivity, with the HL-LHC already being capable of probing the larger di-Higgs cross sections in the SFOEWPT parameter space for $m_2 \lesssim 500$ GeV. A full exploration of the SFOEWPT-compatible parameter space would require $\sqrt{s} \sim 100$ TeV with 30 fb^{-1}.

Our analysis is organized as follows: in Sec. II we establish our notation for the xSM and discuss its basic collider phenomenology. Section III describes the EWPT in the xSM, its related phenomenology and our methodology for choosing benchmark points for di-Higgs production. In Sec. IV, we explore discovery prospects for resonant di-Higgs production for the $b\bar{b}\gamma\gamma$ (Sec. IV A) and 4τ (Sec. IV B) final states, and perform a combination of these two channels in Sec. V. Finally, in Sec. VI, we present our conclusions.

II. THE XSM: MODEL AND COLLIDER PHENOMENOLOGY

In its most general form, the xSM constitutes a framework for simultaneously studying the generic characteristics of singlet scalar driven EWPT dynamics and Higgs portal mediated resonant di-Higgs production. The results of this study can thus be mapped onto other models that may also involve additional degrees of freedom not relevant to either the EWPT or di-Higgs production, $e.g.$ the NMSSM [17, 18]. To make the connection between the EWPT dynamics and resonant di-Higgs production, we study the most general form for the xSM zero temperature potential that depends on the Higgs doublet, H, and real singlet, S (see $e.g.$ [11, 14, 19, 20]):

$$V(H,S) = -\mu^2 \left(H^\dagger H\right) + \lambda \left(H^\dagger H\right)^2 + \frac{a_1}{2}\left(H^\dagger H\right)S$$
$$+ \frac{a_2}{2}\left(H^\dagger H\right)S^2 + \frac{b_2}{2}S^2 + \frac{b_3}{3}S^3 + \frac{b_4}{4}S^4. \quad (2)$$

The a_1 and a_2 parameters constitute the Higgs portal that provides the only connection to the SM for the singlet scalar S. The b_2, b_3, and b_4 parameters are self-interactions that, without the Higgs portal, constitute a hidden sector. In the absence of a_1 and b_3, the potential has a $\mathbb{Z}_2$ symmetry that, if $\langle S \rangle = 0$, stabilizes S and elevates it to the status of a dark matter candidate (for a discussion of this possibility, see $e.g.$ [20–27]). However, as both parameters can play a significant role in the strength of the EWPT, they are retained in the current study, rendering S incapable of acting as a dark matter candidate. For a recent study of the EWPT in the $\mathbb{Z}_2$-symmetric xSM and its signatures at a 100 TeV pp collider, see Ref. [13].

After EWSB, $H \to (v_0 + h)/\sqrt{2}$ with $v_0 = 246$ GeV, and we allow for a possible vacuum expectation value (vev) for S, $i.e.$ $S \to x_0 + s$. Vacuum stability requires the positivity of the quartic coefficients along all directions in field space. Along the h (s) direction, this leads to the bound $\lambda > 0$ ($b_4 > 0$) while, along an arbitrary direction, this implies $a_2 > -\sqrt{\lambda b_4}$. We note that the sign of any term that breaks the $\mathbb{Z}_2$ symmetry can be changed by the field redefinition $S \to -S$. In the Monte Carlo parameter scan that follows, we will allow the $\mathbb{Z}_2$-breaking operator coefficients a_1 and b_3 to take on either sign. Doing so is equivalent to fixing the magnitudes of these parameters and carrying out the $S \to -S$ redefinition. Consequently, we will choose x_0 to be positive without any loss of generality.

The minimization conditions allow for two of the parameters in Eq. (2) to be expressed in terms of the vevs and other parameters. For convenience, we choose

$$\mu^2 = \lambda v_0^2 + (a_1 + a_2 x_0)\frac{x_0}{2}$$
$$b_2 = -b_3 x_0 - b_4 x_0^2 - \frac{a_1 v_0^2}{4x_0} - \frac{a_2 v_0^2}{2}. \quad (3)$$

For viable EWSB, two conditions must be met. The first is that (v_0, x_0) is a stable minimum, which requires

$$b_3 x_0 + 2b_4 x_0^2 - \frac{a_1 v_0^2}{4x_0} - \frac{(a_1 + 2a_2 x_0)^2}{8\lambda} > 0. \quad (4)$$

The second is that the EW minimum must be the absolute minimum, which we impose numerically.

After EWSB, mixing between the states h and s is induced by both the Higgs portal parameters a_1, a_2 and the singlet vev with the mass-squared matrix

$$m_h^2 \equiv \frac{d^2V}{dh^2} = 2\lambda v_0^2$$

$$m_s^2 \equiv \frac{d^2V}{ds^2} = b_3 x_0 + 2b_4 x_0^2 - \frac{a_1 v_0^2}{4x_0}$$

$$m_{hs}^2 \equiv \frac{d^2V}{dhds} = (a_1 + 2a_2 x_0)\frac{v_0}{2}. \qquad (5)$$

with m_{hs}^2 being responsible for the singlet-doublet mixing. The corresponding mass eigenstates are given by

$$h_1 = h\cos\theta + s\sin\theta$$
$$h_2 = -h\sin\theta + s\cos\theta \qquad (6)$$

where h_1 (h_2) is the more $SU(2)_L$-like (singlet-like) scalar and the mixing angle θ is most easily defined in terms of the mass eigenvalues,

$$m_{2,1}^2 = \frac{m_h^2 + m_s^2 \pm |m_h^2 - m_s^2|\sqrt{1 + \left(\frac{m_{hs}^2}{m_h^2 - m_s^2}\right)^2}}{2}, \qquad (7)$$

as

$$\sin 2\theta = \frac{2m_{hs}^2}{(m_1^2 - m_2^2)} = \frac{(a_1 + 2a_2 x_0)\, v_0}{(m_1^2 - m_2^2)}. \qquad (8)$$

The $SU(2)_L$-like scalar eigenstate h_1 is considered the lighter eigenstate and identified with the observed Higgs boson at the LHC [1, 2], so we set $m_1 = 125$ GeV. According to Eq. (6), the couplings of h_1 and h_2 to all SM states are simply rescaled versions of SM Higgs couplings, i.e.,

$$g_{h_1 XX} = \cos\theta\, g_{hXX}^{\rm SM}, \quad g_{h_2 XX} = \sin\theta\, g_{hXX}^{\rm SM} \qquad (9)$$

with XX representing any SM final state. The mixing angle is thus constrained by measurements of Higgs signal strengths, oblique parameters, and direct heavy SM-like Higgs searches. A SFOEWPT requires $m_{hs}^2 < 0$ and correspondingly $\sin 2\theta > 0$.

In this work, we concentrate on the kinematic regime in which resonant di-Higgs production occurs, which we take to be $2m_1 \leq m_2 \leq 1$ TeV. In this case, h_1 has no new scalar decay modes, which implies that all signal rates associated with Higgs measurements are functions of the mixing angle only:

$$\mu_{h_1 \to XX} = \frac{\sigma \cdot \rm BR}{\sigma^{SM} \cdot \rm BR^{SM}} = \cos^2\theta \qquad (10)$$

where σ is the production cross section and BR is the branching ratio (equal to $\rm BR^{SM}$ in the absence of new h_1 scalar decay modes). The current limit from Higgs measurements, obtained by performing a global χ^2 fit to data from both ATLAS and CMS, is $|\cos\theta| \gtrsim 0.85$ [16]. Estimated sensitivities to the mixing angle from future collider experiments may also be obtained using a simple χ^2-method (see [16, 28] for details). As in [16], we derive projected sensitivities for the high luminosity LHC ($\sqrt{s}$ = 14 TeV, 3 ab^{-1}), the ILC (ILC-1: $\sqrt{s}$ = 250 GeV, 250 fb^{-1} and ILC-3: $\sqrt{s}$ = 1 TeV, 1 ab^{-1}), and a future circular e^+e^- collider ($\sqrt{s}$ = 240 GeV, 1 ab^{-1}), shown in Fig. 1 (left) as black, blue, and red vertical lines respectively.

The effects of the xSM on electroweak precision observables and the W-boson mass are characterized by the oblique parameters S, T, and U. From Eq. (6), the shift in any oblique parameter, $\mathcal{O}$, can be written entirely in terms of the SM Higgs contribution to that parameter, $\mathcal{O}^{SM}(m)$, where m is either m_1 or m_2. These shifts then take the form

$$\Delta\mathcal{O} = (\cos^2\theta - 1)\mathcal{O}^{SM}(m_1) + \sin^2\theta\, \mathcal{O}^{SM}(m_2)$$
$$= \sin^2\theta\left(\mathcal{O}^{SM}(m_2) - \mathcal{O}^{SM}(m_1)\right), \qquad (11)$$

where it is clear that the corresponding constraint is significantly enhanced in the high mass region. We take the best fit values for the shifts, $\Delta\mathcal{O}$, from the most recent post-Higgs-discovery electroweak fit to the SM by the Gfitter group [29] and perform a global χ^2 fit, including all correlations, to this data (for details, see [16]). The 95% C.L. allowed region in the $(\cos\theta, m_2)$ plane is shown in Fig. 1 (left) as the beige shaded region.

LHC searches for a heavy SM-like Higgs boson also provide a probe of h_2 since it will decay to all SM Higgs boson decay products as well as to h_1 pairs (for $m_2 > 2m_1$). In particular, the ATLAS [30, 31] and CMS [32, 33] Collaborations have performed searches for SM-like heavy Higgs bosons in the mass range 145-1000 GeV focusing on WW and ZZ final states, placing limits on the corresponding signal rate at the 95% C.L.

All production modes for h_2 are inherited entirely from mixing and, thus, $\sin\theta$ fully controls the production cross section with respect to (w.r.t.) its SM value. In contrast, in the kinematic regime where resonant di-Higgs production is allowed, the new scalar decay mode $h_2 \to h_1 h_1$ yields a modification of all the h_2 branching fractions w.r.t. their SM values. This new decay mode is dependent on the trilinear coupling

$$\lambda_{211} = \frac{1}{4}\Big[(a_1 + 2a_2 x_0)\cos^3\theta + 4v_0(a_2 - 3\lambda)\cos^2\theta\sin\theta$$
$$+ (a_1 + 2a_2 x_0 - 2b_3 - 6b_4 x_0)\cos\theta\sin^2\theta - 2a_2 v_0 \sin^3\theta\Big] \qquad (12)$$

and, along with the $\sin^2\theta$ rescaling, modifies the rate associated with the heavy Higgs production and decay. The partial width $\Gamma_{h_2 \to h_1 h_1}$ is given by

$$\Gamma_{h_2 \to h_1 h_1} = \frac{\lambda_{211}^2 \sqrt{1 - 4m_1^2/m_2^2}}{8\pi m_2}. \qquad (13)$$

Defining $\Gamma^{\mathrm{SM}}(m_2)$ as the SM Higgs width evaluated at m_2, which we take from [34], the total width for the h_2 boson is given by

$$\Gamma_{h_2} = \sin^2\theta\, \Gamma^{\mathrm{SM}}(m_2) + \Gamma_{h_2 \to h_1 h_1}. \qquad (14)$$

The resulting signal rate (normalized to the SM value) for $pp \to h_2 \to XX$ (with XX representing all SM final states except $h_1 h_1$) is

$$\mu_{h_2 \to XX} = \sin^2\theta \left(\frac{\sin^2\theta\, \Gamma^{\mathrm{SM}}(m_2)}{\Gamma_{h_2}} \right). \qquad (15)$$

Due to the implicit dependence on λ_{211}, it is not possible to display the CMS constraint on $\mu_{h_2 \to XX}$ in the form of a smooth region in Fig. 1 (left). However, we apply this constraint at the level of a MC scan (see Sec. III) and find that doing so excludes no additional parameter regions beyond those already ruled out by electroweak precision observables at the 95% C.L.

III. ELECTROWEAK PHASE TRANSITION & BENCHMARKS FOR DI-HIGGS PRODUCTION

The character of the EWPT is understood in terms of the behavior of the finite temperature effective potential, $V_{\mathrm{eff}}^{T \neq 0}$. However, it is well-known that the standard derivation of $V_{\mathrm{eff}}^{T \neq 0}$ suffers from gauge dependence (see [35] for an in-depth review). Although the value of the EWSB vev at the critical temperature, $\phi(T_c)$, is inherently gauge-dependent as it is not an observable, the standard method for extracting T_c also introduces a separate and spurious gauge-dependence. The consequence is that the conventional criterion for avoiding baryon washout, $\phi(T_c)/T_c \gtrsim 1$, inherits both sources. In this work, we employ a high temperature expansion to restore gauge-indepence to our analysis (see [16] for details). This requires forgoing the addition of the $T{=}0$ Coleman-Weinberg 1-loop effective potential as well as retaining only the gauge-independent thermal mass corrections to $V_{\mathrm{eff}}^{T \neq 0}$, which are critical to restoring electroweak symmetry at high temperatures. Within this limit, the T-dependent vevs, T_c, and the bubble nucleation rate are all manifestly gauge-independent. We note here that this limit is particularly suited to the xSM, which generates the required barrier between the broken and unbroken phases at tree-level via the parameters a_1 and b_3.

In the high temperature limit, we follow [36] and write the T-dependent, gauge-independent (indicated by the presence of a bar) vevs in a cylindrical coordinate representation as

$$\bar{v}(T)/\sqrt{2} = \bar{\phi}\cos\alpha(T), \quad \bar{x}(T) = \bar{\phi}\sin\alpha(T). \qquad (16)$$

The energy of the electroweak sphaleron responsible for baryon washout is proportional to the $SU(2)_L$-breaking energy scale, $\bar{v}(T)$. Sufficient quenching of the sphaleron

transitions in the broken phase, in order to preserve any baryon asymmetry against washout, is then characterized by the requirement

$$\cos\alpha(T_c)\frac{\bar{\phi}(T_c)}{T_c} \gtrsim 1. \qquad (17)$$

If this condition is met, then the EWPT is said to be a SFOEWPT. As emphasized in Ref. [35], this criterion is subject to a number of theoretical uncertainties, even in the presence of a gauge-invariant computation as performed here. Consequently, when considering the phenomenological implications resulting from our parameter scan, one should treat constraints imposed by Eq. (17) as approximate.

The critical values, $\bar{\phi}(T_c)$ and $\alpha(T_c)$, are determined by minimizing $V_{\mathrm{eff}}^{T \neq 0}(\phi, \alpha, T)$ while T_c is defined as the temperature at which the broken and unbroken phases are degenerate: $V_{\mathrm{eff}}^{T \neq 0}(\phi, \alpha \neq \pi/2, T_c) = V_{\mathrm{eff}}^{T \neq 0}(\phi, \alpha = \pi/2, T_c)$. We implement the xSM in the high temperature limit in CosmoTransitions [37] to numerically obtain all of the above quantities characterizing the EWPT. Moreover, we calculate the finite temperature thermal tunnelling rate into the electroweak phase, requiring it to be sufficiently fast in order to preclude the possibility of the Universe becoming stuck in a false metastable phase.

With these considerations, we take a_1, b_3, x_0, and b_4 as independent parameters and perform MC scans of the xSM parameter space within the following ranges

$$a_1/\mathrm{TeV}, b_3/\mathrm{TeV} \in [-1, 1], \quad x_0/\mathrm{TeV} \in [0, 1],$$
$$b_4, \lambda \in [0, 1] \qquad (18)$$

where the lower bounds on the quartic couplings ensure vacuum stability. With our choice of independent parameters, both $\cos\theta$ and a_2 are fixed by the parameters of the scan and m_2. Following Ref. [13], we impose a naïve perturbativity bound on the Higgs portal coupling $a_2/2 \lesssim 5$. For each point, we require a SFOEWPT with sufficient tunneling rate as well as consistency with all basic theoretical limits and current bounds from Higgs measurements, electroweak precision observables, and heavy Higgs searches. We present all points that pass these requirements (displayed in black) in the $(\cos\theta, m_2)$ plane in Fig. 1 (left). Further details about the generic parameteric behavior under the above conditions are provided in [16].

We turn now to the analysis of resonant di-Higgs production, beginning with our selection of benchmark points. We focus on gluon fusion, as it is by far the dominant production mechanism within the m_2 range of interest. As already stressed above, xSM di-Higgs production differs considerably from the analogous process in the SM, since the s-channel $gg \to h_2 \to h_1 h_1$ amplitude is resonant for $m_2 > 2\,m_1$, leading to a large enhancement of the production cross section as well as a different kinematic behavior of the full di-Higgs amplitude. In addition, di-Higgs production in the SM and
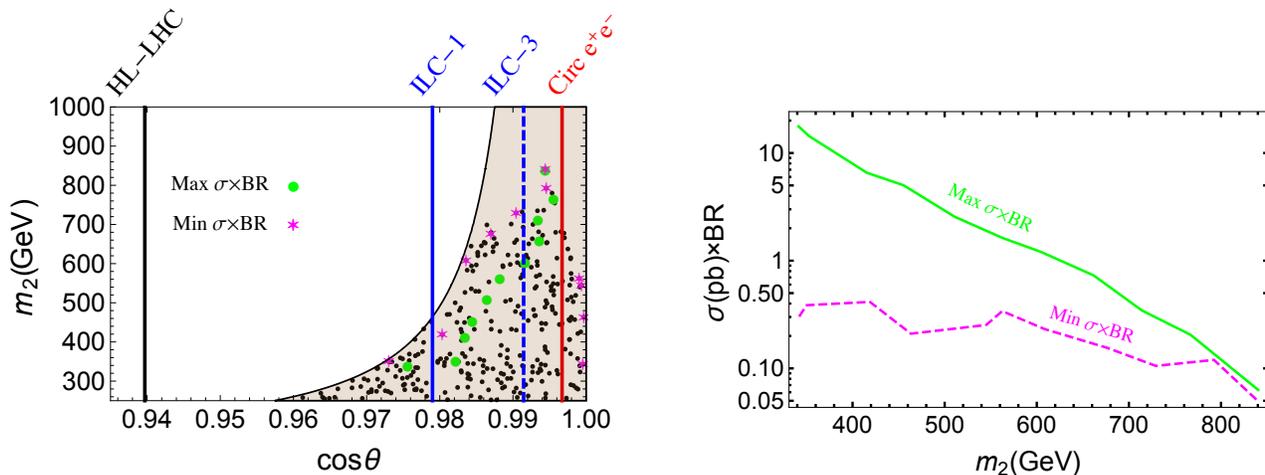
FIG. 1: Left pane: Distribution of SFOEWPT points in m_2 *vs* $\cos\theta$ space. Maximum (minimum) benchmark points are shown in green (magenta). Right pane: Maximum (minimum) cross section times branching ratio as a function of m_2 at a 100 TeV pp collider, taken from Table I (Table II), is displayed as a solid green (dashed magenta) line.

xSM differ in two important ways: *(i)* For the xSM, the 1-loop $gg\,h_2$ interaction is rescaled by $\sin\theta$, leading to a suppression of the cross section by $\sin^2\theta$. *(ii)* The trilinear coupling involved in producing the $h_1 h_1$ final state is different depending on whether h_1 or h_2 is the intermediate state. Moreover, the h_1^3 trilinear coupling λ_{111} in the xSM can also differ significantly from its SM value within the parameter space leading to a SFOEWPT [16].

For $\lambda_{211} = 0$ the branching fractions of h_2 into SM states equal those of a SM Higgs boson with mass m_2 (recall the discussion at the end of Section II). For $\lambda_{211} \neq 0$, the branching fraction for $h_2 \to h_1 h_1$

$$\mathrm{BR}(h_2 \to h_1 h_1) = \frac{\Gamma_{h_2 \to h_1 h_1}}{\Gamma_{h_2}} \qquad (19)$$

incorporates a non-trivial parameter dependence through λ_{211} since the partial width $\Gamma_{h_2 \to h_1 h_1}$ is proportional to λ_{211}^2 (see Eqn. 13).

The resonant di-Higgs cross section is thus given at leading order (LO) by $\sin^2\theta \times \sigma_{\mathrm{LO}}(pp \to h)^{\mathrm{SM}}(m_2) \times \mathrm{BR}(h_2 \to h_1 h_1)$. Following [38], we write $\sigma_{\mathrm{LO}}(pp \to h)^{\mathrm{SM}}(m_2)$ as

$$\sigma_{\mathrm{LO}}(pp \to h)^{\mathrm{SM}}(m_2) = \frac{G_F \, \alpha_s^2}{512\sqrt{2}\pi} \left| \sum_q A_{1/2}\left(\frac{m_2^2}{4m_q^2}\right) \right|^2$$
$$\times \, m_2^2 \, \frac{d\mathcal{L}}{dm_2^2} \qquad (20)$$

where G_F is the Fermi constant, α_s is the strong coupling (evaluated at 100 TeV), and $A_{1/2}$ is the loop function given in [38]. In the case of resonant production, the convolution of parton distribution functions with the LO cross section yields a single parton luminosity function $\frac{d\mathcal{L}}{dm_2^2}$ (given *e.g.* in [34]) for energies $\sqrt{s} = 100$ TeV and Higgs mass values of throughout the m_2 range of interest.

Our results at LO in QCD are expected to be conservative estimates of signal sensitivity, as higher-order contributions, encoded in the relevant k-factors, would increase both signal and background cross sections and increase the sensitivity by $\sim \sqrt{k}$.

Using the results in Eqs. (19) and (20), we choose two sets of benchmark points from our previous MC scan of the xSM parameter space. The first set, labeled BM$^{\mathrm{max}}$, consists of the points that maximize the LO di-Higgs rate in each 50 GeV window within the range $m_2 \in [300\ \mathrm{GeV},$ 1 TeV]. The second set, labeled BM$^{\mathrm{min}}$, is analogous to the first but for points that minimize the LO di-Higgs rate. We show both sets in Fig. 1 (left), with BM$^{\mathrm{max}}$ as green circles and BM$^{\mathrm{min}}$ as magenta stars, and display their numerical values respectively in Tables I and II. Also shown in Fig. 1 (right) are the maximum and minimum cross section times branching ratio as a function of m_2, corresponding to these benchmark points. To guide the reader's eye and indicate the overall trends, we have connected the BM$^{\mathrm{max}}$ (BM$^{\mathrm{min}}$) di-Higgs cross sections with a solid green (dashed magenta) line.

It is worth stressing that it is possible to find highly-tuned points in the xSM parameter space that yield a SFOEWPT while featuring a very fine cancellation among different terms in (12), leading to $\lambda_{211} \to 0$. Such "outlier" points would thus yield a value for $\sigma\times$BR much below a sensible BM$^{\mathrm{min}}$, but they correspond to very tuned corners of the xSM that do not represent the general properties of the model. In our MC scan, these outliers can be identified as yielding a dramatic drop in $\sigma\times$BR with respect to the subsequent BM$^{\mathrm{min}}$ candidate benchmark within each 50 GeV mass window. We have identified and eliminated one such outlier point in favor of the selected BM8$^{\mathrm{min}}$.

We note here that no SFOEWPT-viable points are discovered by the scan above $m_2 \sim 850$ GeV even though it accepts points up to $m_2 = 1$ TeV. Moreover, it is clear

Benchmark	$\cos\theta$	$\sin\theta$	m_2 (GeV)	Γ_{h_2} (GeV)	x_0 (GeV)	λ	a_1 (GeV)	a_2	b_3 (GeV)	b_4	λ_{111} (GeV	λ_{211} (GeV)	σ (pb)	BR
B1	0.976	0.220	341	2.42	257	0.92	-377	0.392	-403	0.77	204	-150	23.9	0.74
B2	0.982	0.188	353	2.17	265	0.99	-400	0.446	-378	0.69	226	-144	19.0	0.76
B3	0.983	0.181	415	1.59	54.6	0.17	-642	3.80	-214	0.16	44.9	82.5	20.1	0.33
B4	0.984	0.176	455	2.08	47.4	0.18	-707	4.63	-607	0.85	46.7	93.5	16.3	0.31
B5	0.986	0.164	511	2.44	40.7	0.18	-744	5.17	-618	0.82	46.6	91.9	10.8	0.24
B6	0.988	0.153	563	2.92	40.5	0.19	-844	5.85	-151	0.083	47.1	104	6.96	0.23
B7	0.992	0.129	604	2.82	36.4	0.18	-898	7.36	-424	0.28	45.6	119	4.01	0.30
B8	0.994	0.113	662	2.97	32.9	0.17	-976	8.98	-542	0.53	44.9	132	2.23	0.33
B9	0.993	0.115	714	3.27	29.2	0.18	-941	8.28	497	0.38	44.7	112	1.73	0.20
B10	0.996	0.094	767	2.83	24.5	0.17	-920	9.87	575	0.41	42.2	114	0.918	0.22
B11	0.994	0.105	840	4.03	21.7	0.19	-988	9.22	356	0.83	43.9	83.8	0.802	0.079

TABLE I: Values of the various xSM independent and dependent parameters for each of the benchmark values chosen to **maximize** the $\sigma \cdot BR(h_2 \to h_1 h_1)$ at a 100 TeV pp collider. These values are represented as green circular points in Fig. 1 (left) and as the solid green curve in Fig. 1 (right).

Benchmark	$\cos\theta$	$\sin\theta$	m_2 (GeV)	Γ_{h_2} (GeV)	x_0 (GeV)	λ	a_1 (GeV)	a_2	b_3 (GeV)	b_4	λ_{111} (GeV	λ_{211} (GeV)	σ (pb)	BR
B1	0.999	0.029	343	0.041	105	0.13	-850	3.91	-106	0.29	32.1	19.3	0.428	0.72
B2	0.973	0.231	350	0.777	225	0.18	-639	0.986	-111	0.97	37.7	11.6	27.8	0.014
B3	0.980	0.197	419	1.32	234	0.18	-981	1.56	0.42	0.96	39.0	17.5	23.5	0.018
B4	0.999	0.026	463	0.0864	56.8	0.13	-763	6.35	113	0.73	32.2	27.4	0.334	0.63
B5	0.999	0.035	545	0.278	50.2	0.13	-949	8.64	151	0.57	33.0	51.6	0.408	0.62
B6	0.999	0.043	563	0.459	33.0	0.13	-716	9.25	-448	0.96	33.7	66.8	0.553	0.62
B7	0.984	0.180	609	4.03	34.2	0.22	-822	4.53	-183	0.57	47.8	45.2	7.67	0.030
B8	0.987	0.161	676	4.47	30.3	0.22	-931	5.96	-680	0.43	48.4	55.2	4.17	0.037
B9	0.990	0.138	729	4.22	27.3	0.21	-909	6.15	603	0.93	45.7	61.0	2.33	0.045
B10	0.995	0.104	792	3.36	22.2	0.18	-936	9.47	-848	0.66	43.5	92.4	0.991	0.12
B11	0.994	0.105	841	3.95	21.2	0.19	-955	8.69	684	0.53	43.3	73.4	0.801	0.062

TABLE II: Values of the various xSM independent and dependent parameters for each of the benchmark values chosen to **minimize** the $\sigma \cdot BR(h_2 \to h_1 h_1)$ at a 100 TeV pp collider. These values are represented as magenta star-shaped points in Fig. 1 (left) and as the dashed magenta curve in Fig. 1 (right).

from Fig. 1 (left) that (i) prospective circular e^+e^- colliders are expected to have the ability to probe all benchmark points in BM$^{\text{max}}$; (ii) the ILC could probe up to BM8$^{\text{max}}$; and (iii) neither e^+e^- collider option has the capability of excluding the full SFOEWPT-viable xSM parameter space. In short, many points in BM$^{\text{min}}$ lie beyond the sensitivity reach of presently envisioned, future e^+e^- colliders. In the next section, we show that there are options for future pp colliders in the 100 TeV range that would be capable of discovering not only the benchmarks of BM$^{\text{max}}$ but also those of BM$^{\text{min}}$, rendering the entire SFOEWPT-viable xSM parameter space discoverable.

IV. MONTE CARLO SIMULATIONS

The prospective final states for searching for di-Higgs production are reproduced from [39] in Table VIII, ranked by branching ratio. In this table, the gauge bosons are required to decay to leptons to suppress enormous backgrounds from QCD jet production. QCD production of b-jets and $t\bar{t}$ respectively will likely overwhelm the $4b$ channel[2], as well as make the $b\bar{b}\tau\tau$ and $b\bar{b}W^+W^-$ ($W \to \ell\nu$) channels challenging. Motivated by these considerations, we study the $b\bar{b}\gamma\gamma$ and 4τ final states, which are complementary having different backgrounds

---

[2] As discussed in [40], for $m_2 \gg 1$ TeV this may no longer be the case, but those values of m_2 do not yield a SFOEWPT.

and mass resolution, and discuss the combined results in Sec. V.

After applying kinematic and fiducial cuts, we use the expected signal and background event rates and distributions to estimate the discovery potential of a future 100-TeV scale pp collider. We make use of the MADGRAPH5_AMC@NLO [41] event generator for the hard scattering at leading order (LO) in QCD, and PYTHIA8 [42, 43] for QCD showering, fragmentation and hadronization. The MSTW2008LO68CL [44] parton distribution function (PDF) set was used. The key detector effects are parameterized based on the performance achieved by the LHC experiments; the identification efficiency of photons, b-jets and τ leptons, and the energy resolution of photons and b-jets. In the future, these performance characteristics can serve as benchmarks for the design and simulation of future collider detectors.

The Monte Carlo samples used in this study are stored in the PROMC file format [45, 46] which is analyzable via ROOT [47]. The anti-k_T algorithm [48] is used to reconstruct jets with the FASTJET package [49] and a distance parameter of 0.4. Stable particles (mean lifetimes greater than $3 \cdot 10^{-11}$ seconds) are selected for jet clustering, and neutrinos are excluded.

Optimization of signal and background separation is achieved by employing the boosted decision tree (BDT) algorithm from the toolkit for multivariate analysis class of ROOT [47] and our results are given in terms of a corresponding gaussian significance (N_σ) for rejecting the background-only hypothesis.

A. The $b\bar{b}\gamma\gamma$ Final State

Here we present the analysis for the $b\bar{b}\gamma\gamma$ final state for the benchmarks from Tables I and II.

For the backgrounds, all SM amplitudes contributing to the $\gamma\gamma b\bar{b}$ final state as well as the $\gamma\gamma t\bar{t}$ final state were included. This covers the following processes; $h(\to b\bar{b})h(\to \gamma\gamma)$, $b\bar{b}h(\to \gamma\gamma)$, $Z(\to b\bar{b})h(\to \gamma\gamma)$, $t\bar{t}h(\to \gamma\gamma)$, and non-resonant $b\bar{b}\gamma\gamma$ and $t\bar{t}\gamma\gamma$. These processes have been shown to be the dominant contributors of $b\bar{b}\gamma\gamma$ events in the measurement of the trilinear Higgs self-coupling via Higgs pair production [50, 51]. It is also shown in [50, 51] that backgrounds with jets misidentified as photons or b-jets contribute at most 25% of the total background. Since the mis-identification backgrounds are non-resonant, we neglect these backgrounds with the understanding that they would degrade the sensitivity by $\mathcal{O}(10)\%$. Other neglected effects such as higher-order QCD k-factors would compensate by enhancing the sensitivity by a similar amount.

The following cuts were applied at the generator-level: pseudorapidity $|\eta(\gamma) < 4|$, $|\eta(b) < 4|$, $p_T(\gamma) > 20$ GeV, $p_T(b) > 20$ GeV, $p_T^{\text{leading}}(\gamma) > 40$ GeV, $p_T^{\text{leading}}(b) > 40$ GeV, and the mass cuts $120 < m(\gamma\gamma) < 130$ GeV, $40 < m(b\bar{b}) < 200$ GeV. The visible cross sections with these requirements are presented in Tables IV and V of

Sec. VII. The efficiency for photon [1, 2, 52] and b-quark identification [53–55] was taken to be 75% each [56, 57]. Photon energies were smeared by the electromagnetic calorimeter resolution $20\%/\sqrt{E_T(\gamma)} \oplus 0.17\%$ [1, 2, 52, 58] and b-jet energies were smeared by the hadronic calorimeter resolution $100\%/\sqrt{E_T(b)}$ [56, 57, 59, 60].

A number of variables are computed whose distributions have different shapes for signal and background processes. The decay polar angle θ^* of the h_2 boson in its rest frame, with respect to the beam axis, reflects its scalar nature via a uniform distribution in $\cos\theta^*$. The reconstructed invariant masses of the h_1 bosons and the h_2 boson show characteristic peaks compared to the smooth background distributions. The scalar sum $H_T = \Sigma|\vec{p_T}|$ of all visible objects excluding the h_2 decay products, is sensitive to additional jets in $t\bar{t}$ events. The magnitude of the vector sum $\not{E}_T = |\Sigma\vec{p_T}|$ of all detected objects, which defines the missing transverse energy, can also be large in $t\bar{t}$ events.

We also compare the distributions of the sphericity [61, 62] and the planarity [61, 62] of the event, as computed from the two photons and the two b-jets. In the rest frame of the reconstructed di-Higgs resonance, the sphericity tensor is defined as $S^{\alpha\beta} = (\Sigma_i p_i^\alpha p_i^\beta)/(\Sigma_i|p_i|^2)$, where $\alpha, \beta \in \{x, y, z\}$ and the sums run over the momentum 3-vectors of the two photons and the two b-jets. The eigenvalues $\lambda_{1,2,3}$ of $S^{\alpha\beta}$ represent the fractional squared momenta along three orthogonal eigen-directions, and satisfy the condition $\lambda_1 + \lambda_2 + \lambda_3 = 1$. Ranking the eigenvalues as $\lambda_1 \geq \lambda_2 \geq \lambda_3$, the sphericity is defined as $\frac{3}{2}(\lambda_2 + \lambda_3)$ and the planarity is defined as $(\lambda_2 - \lambda_3)$. An event with large λ_1 has most of the momentum flowing along the major axis of the ellipsoid and little momentum flowing in its two perpendicular directions, leading to a pencil-like event and a small value of sphericity. On the other hand, an event with comparable momentum flow along at least two orthogonal directions leads to higher values of sphericity. In the latter case, if λ_3 is small, the momentum flow is confined to two orthogonal directions defining a plane, yielding a high value of planarity since there is little momentum flow out of the plane.

The distributions of the reconstructed 4-body invariant mass of the $b\bar{b}\gamma\gamma$ system, M_{vis}, and the p_T of the leading decay object (from amongst the two photons and the two b-jets), are shown in Fig. 2 for BM10$^{\text{max}}$ after applying the following additional selection requirements; $115 < m(\gamma\gamma) < 135$ GeV and $40 < m(b\bar{b}) < 200$ GeV. The other distributions mentioned above are shown in Fig. 7 of Sec. VII.

We combine the information in the following distributions: p_T of the leading and sub-leading objects (photons and b-jets), the $\not{E}_T$, the H_T, di-photon mass, $b\bar{b}$-mass, the $\gamma\gamma b\bar{b}$ mass, the sphericity, planarity and $\cos\theta^*$ using a BDT algorithm to separate the $h_2 \to h_1 h_1 \to \gamma\gamma b\bar{b}$ signal from the $\gamma\gamma b\bar{b}$ and $\gamma\gamma t\bar{t}$ backgrounds. The resulting distributions of the BDT score are shown in Fig. 2. For optimal sensitivity, the distribution of the BDT score is binned such that each bin contributes the maximum
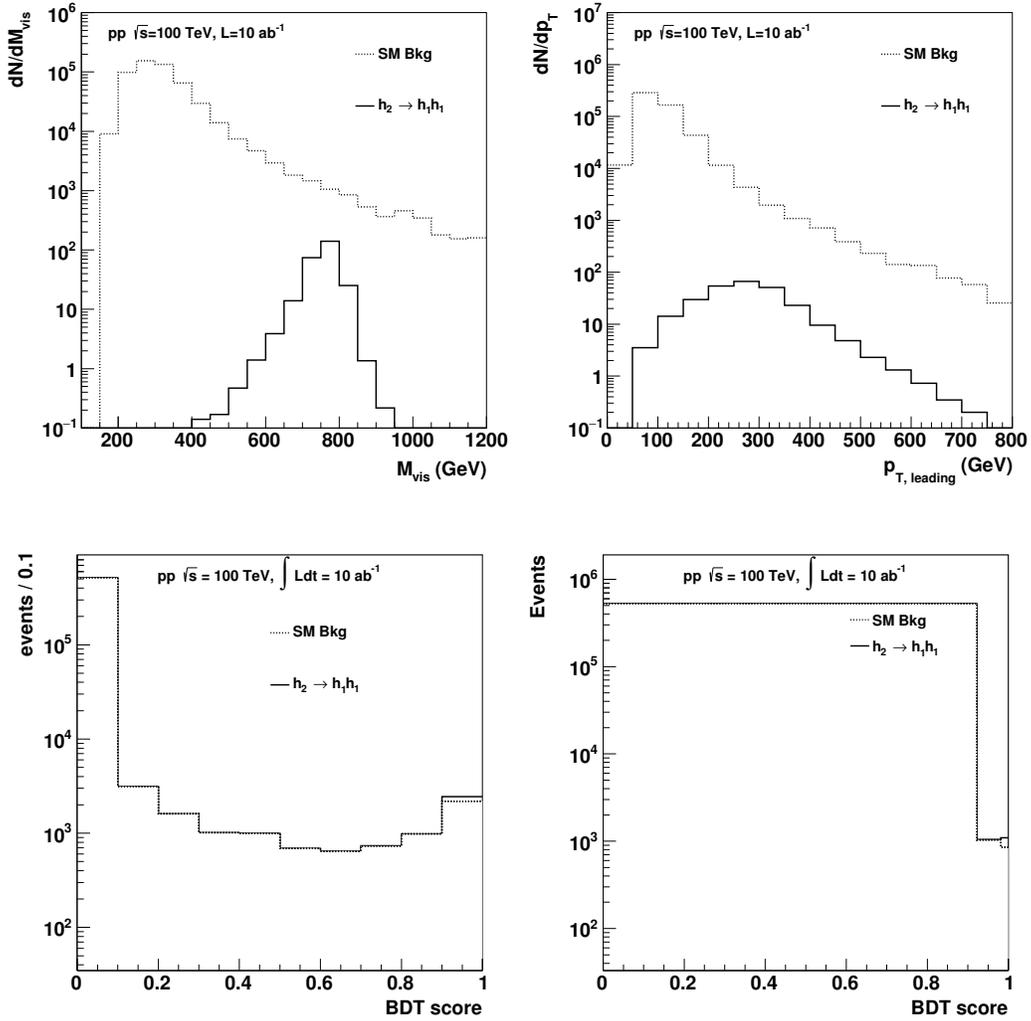
FIG. 2: Signal and background distributions for the $b\bar{b}\gamma\gamma$ final state. The signal distributions correspond to BM10$^{\text{max}}$. The kinematic quantities shown are (top left) the invariant mass of the $b\bar{b}\gamma\gamma$ system, and (top right) the p_T of the leading particle from among the photons and the b-quarks. Also shown are the distributions of the BDT output with uniform binning (bottom left) and optimized binning (bottom right).

FIG. 3: The N_σ gaussian significance for rejecting the background-only hypothesis, obtained using the $b\bar{b}\gamma\gamma$ final state, for each benchmark point. Different collider scenarios of energy and integrated luminosity are compared. The vertical range corresponds to the maximum and minimum signal cross sections in the h_2 mass window.

poisson sensitivity, starting from the right edge of the his-   togram where the signal peaks. With this rebinned his-

togram (Fig. 2), we quantify the discovery reach for the signal by computing the quantity $CL_b = P(Q < Q_{obs}|b)$, the probability for the test-statistic Q to be smaller than the observed value given the background-only hypothesis. When $1 - CL_b < 2.8 \times 10^{-7}$ the background-only hypothesis is rejected at 5σ significance. We convert this background fluctuation probability $1 - CL_b$ into the corresponding N_σ gaussian significance and display them in Sec. VII of the appendix (Tables IV and V).

Here we present these results in Fig. 3, where the shaded colored bands indicate the N_σ ranges spanned by the BM$^{\mathrm{max}}$ and BM$^{\mathrm{min}}$ benchmark points. In Fig. 3 (left) we compare the reach of the HL-LHC with a $\sqrt{s} = 100$ TeV pp collider for two different values of integrated luminosity. Fig. 3 (right) gives the comparison of three different prospective pp collider energies for 30 ab^{-1} of integrated luminosity. It is evident from Fig. 3 (left) that for the $b\bar{b}\gamma\gamma$ channel, the HL-LHC could achieve discovery for a portion of the SFOEWPT-viable parameter space for lower values of m_2, while a 100 TeV future collider with 30 ab^{-1} could enable discovery over essentially all of the SFOEWPT-viable region. While the small region of phase space in the vicinity of the BM11 benchmark point ($m_2 > 820$ GeV) is below the 5σ significance threshold with the $b\bar{b}\gamma\gamma$ channel alone, the combination with another powerful channel using the 4τ final state renders this region also discoverable, as shown below.

B. The 4τ Final State

Here we present the analysis for the 4τ final state for the benchmarks from Tables I and II.

Our background estimates include the SM processes producing four prompt τ-leptons as these are expected to be the dominant sources of backgrounds. Misidentification backgrounds will be suppressed to a negligible level as long as the future collider detectors achieve a τ-identification efficiency and QCD jet rejection rate that are at least as high as the LHC experiments. For example, the ATLAS experiment reports 60% efficiency for the identification of the hadronic decays of the τ-lepton, with a QCD jet efficiency of 1-2% [63]. Based on the construction of highly-granular electromagnetic calorimeters in the future, we assume an overall τ-lepton identification efficiency of 75%, inclusive of all decay channels. We emphasize this benchmark detector performance for hadronic decays, which not only dominate the branching ratios but also provide the narrowest reconstructed Higgs and di-Higgs mass peaks due to the presence of fewer neutrinos in the final state.

It is shown in the $Z' \to \tau\tau$ search [64], where the transverse momenta (p_T) of the τ-leptons are similar to our signal kinematics, that the dominant background in the double-hadronic mode arises from the $\gamma^*/Z \to \tau\tau$ Drell-Yan process. The multijet and W/Z+jet backgrounds are a factor of 3-4 smaller. The dominant background for our $HH \to 4\tau$ search is the $ZZ \to 4\tau$ process. The diboson analysis for $ZV \to \ell\ell jj$ [65] shows that the Z+jets rate is about 20-50 times larger than the VV rate when the $Z \to \ell\ell$ and $V \to jj$ masses are close to the Z or W boson masses. On the other hand, the hadronic τ-lepton selection suppresses QCD jets by a factor of 15 relative to prompt τ-leptons. Thus, the requirement of two additional τ's will suppress the Z+jets background to a fraction of the ZZ background. Background from multi-jets, diboson+dijet and single-top+dijet processes will be suppressed even more strongly. Reference [65] also shows that the $t\bar{t}$ background is negligible when the bosons have high p_T. Thus, the inclusion of the SM 4τ background processes suffices for the estimation of the $h_1 h_1 \to 4\tau$ resonance sensitivity.

Signal and background processes are generated with requirements $p_T(\tau) > 20$ GeV, $p_T^{\mathrm{leading}}(\tau) > 40$ GeV and $|\eta(\tau)| < 4$. The visible cross sections with these requirements are presented in Tables VI and VII of Sec. VIII. Distributions of the signal (BM10$^{\mathrm{max}}$) and background processes for the 4τ final state are shown in Fig. 4. Additional distributions are shown in Fig. 8. As with the $\gamma\gamma b\bar{b}$ channel, we use a number of kinematic quantities computed with the 4τ final state as inputs to a BDT; the invariant mass of the four τ-leptons, the average di-τ mass (to distinguish between $Z \to \tau\tau$ and $h_1 \to \tau\tau$), $\cos\theta^*$, the sphericity and planarity of the event, p_T of the leading and next-to-leading τ-leptons, the $\not{E}_T$ and the H_T, to distinguish the $h_2 \to h_1 h_1 \to 4\tau$ signal from the SM backgrounds. The resulting distribution of the BDT output is shown in Fig. 4. Again, we use the optimally-binned distribution of the BDT output to calculate the N_σ gaussian significance of excluding the background-only hypothesis. We present the results from the 4τ channel in Tables VI and VII of the appendix in Sec VIII and, here, display these results in Fig. 5.

V. COMBINED RESULTS

The results presented in the previous section show that similar sensitivities to the $h_2 \to h_1 h_1$ process are obtained from the $\gamma\gamma b\bar{b}$ and 4τ channels. In the $\gamma\gamma b\bar{b}$ channel, the most discriminating variables are the diphoton and $b\bar{b}$ masses, the 4-body invariant mass, the event sphericity and planarity, and the p_T of the leading objects. The signal events have small sphericity and planarity compared to the backgrounds, due to the back-to-back decays of two h_1 bosons from a massive h_2 boson. In the 4τ channel, the sphericity and the planarity values are also significantly smaller for signal than for backgrounds. The 4τ mass and the average di-τ mass distributions peak at higher mass for signal events, as do the p_T for the leading τ leptons. The H_T and missing E_T variables also provide some discrimination as these variables have higher values for signal events.

Here we present our final results, which compare the discovery potential for resonant di-Higgs pair production for various future collider scenarios in probing the xSM.

FIG. 4: Signal and background distributions for the 4τ final state, where the signal corresponds to BM10$^{\text{max}}$. The kinematic quantities shown are (top left) the invariant mass of the 4τ system, and (top right) the average di-τ pair mass in the event. Also shown are the distributions of the BDT output with uniform binning (bottom left) and optimized binning (bottom right).
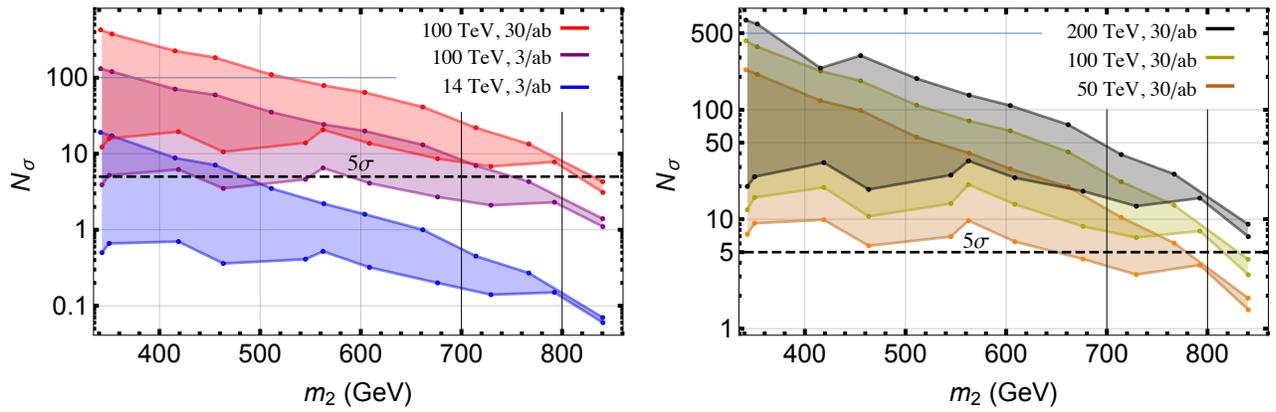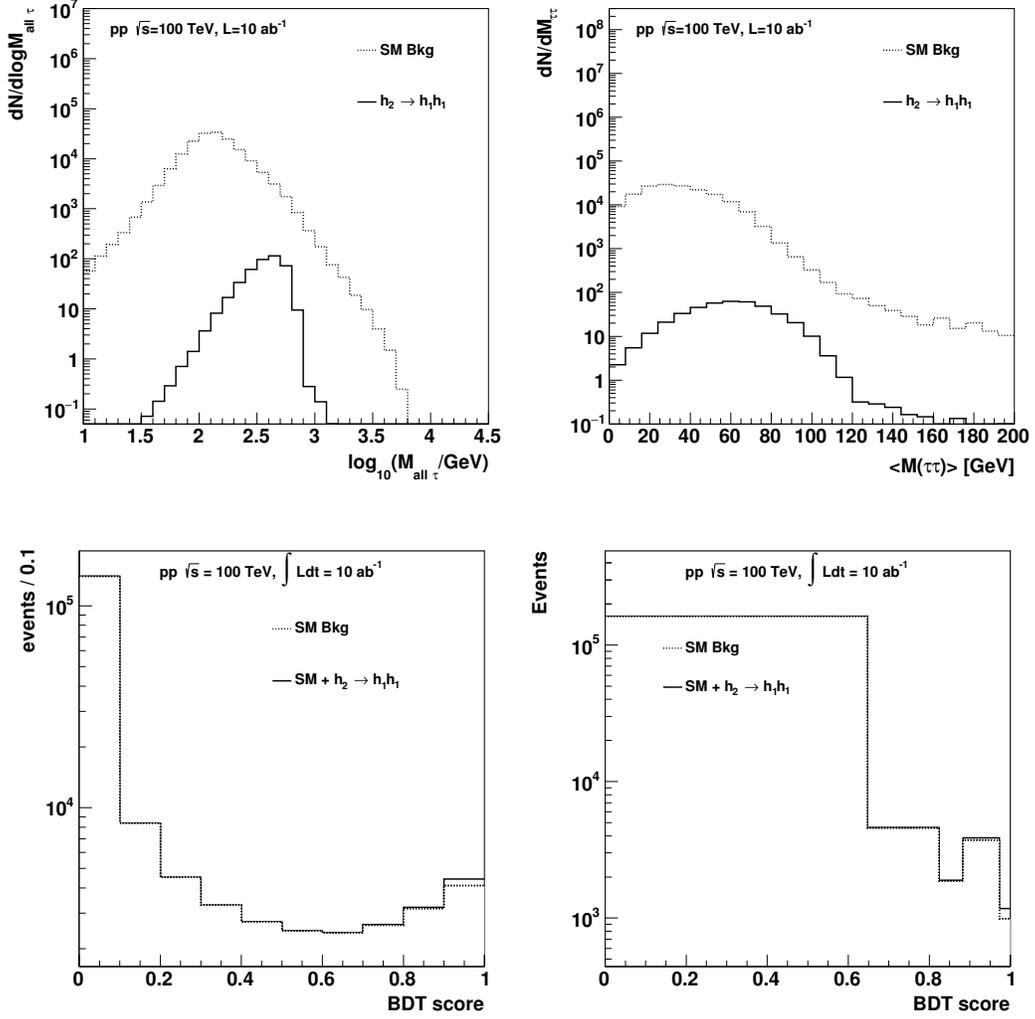

FIG. 5: The N_σ gaussian significance for rejecting the background-only hypothesis, obtained using the 4τ final state, for each benchmark point. Different collider scenarios of energy and integrated luminosities are compared. The vertical range corresponds to the maximum and minimum signal cross sections in the h_2 mass window.

The final results are obtained by combining the N_σ sensitivities of the $\gamma\gamma b\bar{b}$ and 4τ channels. The combination is performed by adding the respective N_σ values in quadrature. The combined sensitivity is shown in Fig. 6 and in
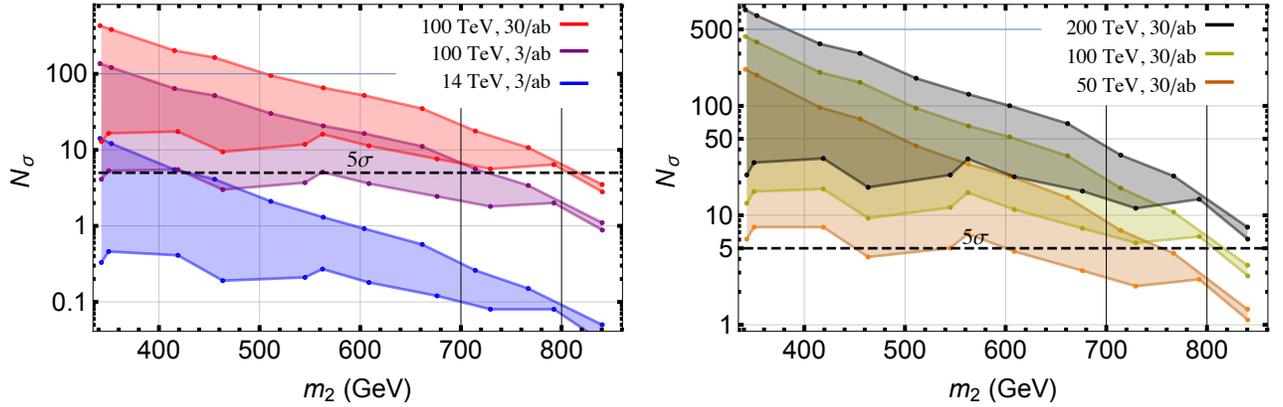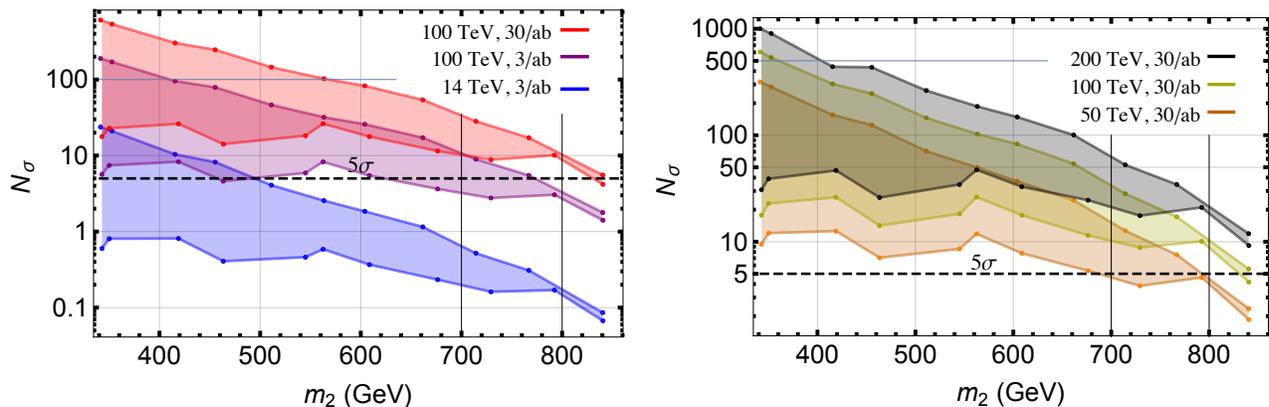
FIG. 6: The N_σ gaussian significance for rejecting the background-only hypothesis, obtained using the combination of the $b\bar{b}\gamma\gamma$ and 4τ final states, for each benchmark point. Different collider scenarios of energy and integrated luminosities are compared. The vertical range corresponds to the maximum and minimum signal cross sections in the h_2 mass window.

TABLE III: Combined results for the sensitivity N_σ to $h_2 \to h_1 h_1$ production from the combination of $b\bar{b}\gamma\gamma$ and 4τ final states. The range ($N_\sigma^{\max}$ - $N_\sigma^{\min}$) indicates the variation in sensitivity that occurs when the signal cross section takes on its minimum and maximum allowed values within the range of parameter space that admits a SFOEWPT.

| | 14 TeV | | 50 TeV | | 100 TeV | | | | | | 200 TeV | |
| | 3 ab^{-1} | | 30 ab^{-1} | | 3 ab^{-1} | | 10 ab^{-1} | | 30 ab^{-1} | | 30 ab^{-1} | |
	$N_\sigma^{\min}$	$N_\sigma^{\max}$	$N_\sigma^{\min}$	$N_\sigma^{\max}$	$N_\sigma^{\min}$	$N_\sigma^{\max}$	$N_\sigma^{\min}$	$N_\sigma^{\max}$	$N_\sigma^{\min}$	$N_\sigma^{\max}$	$N_\sigma^{\min}$	$N_\sigma^{\max}$
B1	0.6	23.7	9.5	316	5.6	189	10.3	347	17.7	606	30.7	1001
B2	0.8	21.0	12.0	284	7.4	170	13.6	313	22.8	537	38.9	902
B3	0.81	10.4	12.6	155	8.3	95.4	15.2	175	26.1	303	46.6	440
B4	0.41	8.2	7.1	124	4.6	78.8	8.4	143	14.2	246	25.9	434
B5	0.46	4.1	8.5	70.9	5.9	46.4	10.9	82.7	18.2	145	34.4	263
B6	0.58	2.5	11.8	49.7	8.3	31.9	14.3	58.1	26.2	103	47.3	186
B7	0.36	1.8	7.8	36.8	5.4	25.8	10.1	47.0	17.7	82.6	32.8	148
B8	0.23	1.2	5.3	24.5	3.6	17.2	6.7	30.4	11.5	54.0	24.5	100
B9	0.16	0.52	3.8	12.7	2.7	8.9	5.0	16.2	8.8	28.2	17.5	52.7
B10	0.17	0.31	4.6	7.5	3.0	5.5	5.8	9.9	10.1	17.1	21.0	34.5
B11	0.07	0.08	1.8	2.3	1.4	1.8	2.4	3.1	4.2	5.5	9.2	11.9

Table III.

As mentioned earlier, the SFOEWPT-viable parameter space has a maximum $m_2 \sim 850$ GeV. We find that with 30 ab^{-1} of integrated luminosity, a 50 TeV pp collider can achieve 5σ discovery of BM10 and lower h_2 masses, but falls short of discovering BM11. With the same integrated luminosity, a 100 TeV collider reaches the 5σ threshold for BM11, and a 200 TeV collider achieves 10σ sensitivity for the same. Thus, the higher collider energies (or correspondingly higher integrated luminosities at lower energies) are needed to discover the $h_2 \to h_1 h_1$ process for $800 < m_2 < 850$ GeV, but the lower mass range can be discovered by lower energy colliders.

We also note that a 100 TeV collider can discover up to BM7, and slices of the parameter space up to BM10, with 3 ab^{-1} of integrated luminosity. Thus, increasing the integrated luminosity to 30 ab^{-1} enables the discovery in the $600 < m_2 < 850$ GeV mass range.

VI. CONCLUSIONS

Exploring the thermal history associated with EWSB is an important task for high energy physics. While EWSB in the SM with a 125 GeV Higgs boson is known to occur through a crossover transition, the addition of a single real gauge-singlet scalar to the scalar potential can significantly alter this picture. For a rather broad range of parameter choices in this simplest extension, EWSB may occur through a strong first order phase transition, thereby providing the out-of-equilibrium environment re-

quired for electroweak baryogenesis. In this context, it is interesting to determine the degree to which the LHC and prospective future high energy colliders might probe the SFOEWPT-viable parameter space of the "xSM".

In this study, we have attempted to address this question by considering parameter space regions that also allow for resonant di-Higgs production in pp collisions. In doing so, we have identified a set of 22 SFOEWPT-viable benchmark parameter sets whose associated di-Higgs cross sections bracket the range of possible values in each of eleven 50 GeV-wide mass bins for the singlet-like scalar, h_2. Focusing on the HL-LHC and representative scenarios for higher-energy pp colliders, we considered the corresponding reach of searches with the $b\bar{b}\gamma\gamma$ and 4τ final states. We then asked: What would be the optimal center of mass energy and integrated luminosity for probing the SFOEWPT in the xSM? Our conclusions, to reprise the introductory discussion, are that:

- There exists interesting discovery potential for the HL-LHC for $m_2 \lesssim 500$ GeV and exclusionary reach to somewhat higher masses

- A 100 (200) TeV pp collider with 30 ab^{-1} of integrated luminosity could probe nearly all (all) of the SFOEWPT-viable parameter space.

- A 50 TeV pp collider with the same integrated luminosity would significantly extend the LHC reach, but would have a limited ability to probe the highest m_2 region.

- Should future precision Higgs boson studies constrain the singlet-doublet mixing angle $|\theta| \lesssim 0.08$ (the currently projected limit from future circular e^+e^- colliders), there would still exist parameter choices for the xSM yielding a SFOEWPT. A future pp collider as discussed here could discover the xSM even in this case.

- The gain in signal significance as a function of integrated luminosity $\mathcal{L}$ and collider energy can be summarized as follows. The signal significance increases with $\mathcal{L}$ as $\sqrt{\mathcal{L}}$ because the statistical fluctuations of both signal and background event yields are gaussian-distributed. The increase of collider energy from 50 TeV to 100 TeV increases the signal significance by a factor of 1.9 (2.3) at the low (high) mass benchmark points. For an increase of collider energy from 100 TeV to 200 TeV, the corresponding increase in signal significance is a factor of 1.7 (2.1). Thus, a factor of four in integrated luminosity is roughly equivalent to a factor of two in collider energy, in terms of sensitivity to the $h_2 \to h_1 h_1$ process at a given h_2 mass.

It is important to take these conclusions somewhat impressionistically, as we have made a number of simplifying assumptions in order to paint the broad picture.

- Theoretically, we have carried out a gauge-invariant analysis of the EWPT by working in the high-T effective theory and omitting the $T = 0$ Coleman-Weinberg contributions to the effective potential. Inclusion of the latter will, in general, yield additional parameter space regions consistent with a SFOEWPT. Moreover, the approximate criteria for baryon number preservation in Eq. (17) is subject to additional theoretical uncertainties, some of which may be remedied with a future Monte Carlo study of the xSM phase transition dynamics.

- Experimentally, we have considered a detector performance similar to the LHC detectors but extended up to $|\eta| < 4$, which is the goal for future collider detector design. We find that the $b\bar{b}\gamma\gamma$ and 4τ final states have equal sensitivities for probing resonant di-Higgs production. The conclusions presented above are based on the combination of the sensitivities from these channels, and emphasize the importance of achieving high acceptance and efficiency for photons, b-jets and hadronic τ-leptons.

With these considerations, we believe that our study provides a reasonable guide to what may be possible with a higher energy pp collider and how it may compare with the HL-LHC. Moreover, for both the LHC and a future collider, the reach may be enhanced by considering other final states not studied here. For these reasons, the opportunities with a 100 TeV collider appear to be quite promising. Additional investigation of the energy frontier as a probe of the EWPT, thus, appears well worth the effort.

VII.   APPENDIX A: $b\bar{b}\gamma\gamma$ ANALYSIS

In this section, we display the remaining kinematic distributions used in our BDT analysis which were not included in the main text of section IV A. We also include here tables of cross sections and N_σ results from our BDT analysis for the sets of benchmark points yielding the maximum and minimum signal cross sections.

FIG. 7: Additional kinematics distributions for $b\bar{b}\gamma\gamma$ final state, used as inputs to the BDT. The signal distributions correspond to BM10$^{\mathrm{max}}$.

TABLE IV: Cross sections and BDT analysis results for $b\bar{b}\gamma\gamma$ final state, for benchmark points yielding the maximum signal cross section.

	14 TeV		50 TeV		100 TeV				200 TeV	
		3 ab^{-1}		30 ab^{-1}		3 ab^{-1}	10 ab^{-1}	30 ab^{-1}		30 ab^{-1}
	σ_{XS} (ab)	N_σ	σ_{XS} (ab)	N_σ	σ_{XS} (ab)	N_σ	N_σ	N_σ	σ_{XS} (ab)	N_σ
Background	72,400		505,500		1,323,000				3,268,000	
B1	355	19.1	4,230	231	12,700	131	241	426	34,200	658
B2	284	17.2	3,460	211	10,500	120	223	376	28,400	607
B3	93	8.8	1,260	121	3,990	70.8	131	226	11,100	240
B4	59.6	7.1	865	98.7	2,790	59.4	108	184	7,900	313
B5	24.7	3.5	391	56.3	1,300	35.3	63.5	110	3,800	193
B6	13.6	2.2	233	40.1	799	24.3	43.7	79.0	2,380	136
B7	8.9	1.6	162	28.9	568	19.9	36.1	64.2	1,700	109
B8	4.7	1.0	92.6	19.7	334	13.1	24.1	41.2	1,000	73.1
B9	2.0	0.45	41.6	10.4	154	7.0	13.0	22.0	484	39.0
B10	1.0	0.27	23.1	6.0	87.2	4.3	8.1	13.4	279	25.9
B11	0.27	0.07	6.7	1.9	26.1	1.4	2.4	4.3	85.6	9.0

TABLE V: Cross sections and BDT analysis results for the $b\bar{b}\gamma\gamma$ final state, for benchmark points yielding the minimum signal cross section.

| | 14 TeV | | 50 TeV | | 100 TeV | | | | 200 TeV | |
| | | 3 ab^{-1} | | 30 ab^{-1} | | 3 ab^{-1} | 10 ab^{-1} | 30 ab^{-1} | | 30 ab^{-1} |
	σ_{XS} (ab)	N_σ	σ_{XS} (ab)	N_σ	σ_{XS} (ab)	N_σ	N_σ	N_σ	σ_{XS} (ab)	N_σ
Background	72,400		505,500		1,323,000				3,268,000	
B1	6.3	0.50	75.2	7.3	230	3.9	7.1	12.2	610	19.9
B2	7.8	0.66	94.8	9.2	287	5.2	9.8	15.8	775	24.4
B3	5.8	0.70	79.4	9.9	250	6.2	11.4	19.5	702	32.9
B4	2.4	0.36	35.8	5.7	116	3.5	6.5	10.6	331	18.8
B5	2.2	0.41	37.2	6.9	127	4.6	8.5	13.9	374	25.4
B6	2.8	0.52	49.1	9.6	170	6.5	10.9	20.7	501	34.1
B7	1.7	0.32	30.9	6.2	110	4.1	7.7	13.7	328	23.9
B8	0.97	0.20	19.4	4.3	70.5	2.7	5.0	8.6	220	18.0
B9	0.58	0.14	12.5	3.1	46.6	2.1	3.9	6.8	147	13.2
B10	0.56	0.15	13.2	3.8	50.4	2.3	4.5	7.8	163	15.5
B11	0.21	0.06	5.2	1.5	20.4	1.1	1.8	3.1	66.9	6.9

VIII.   APPENDIX B: 4τ ANALYSIS

In this section, we display the remaining kinematic distributions used in our BDT analysis which were not included in the main text of section IV B. We also include here tables of cross sections and N_σ results from our BDT analysis for the sets of benchmark points yielding the maximum and minimum signal cross section.
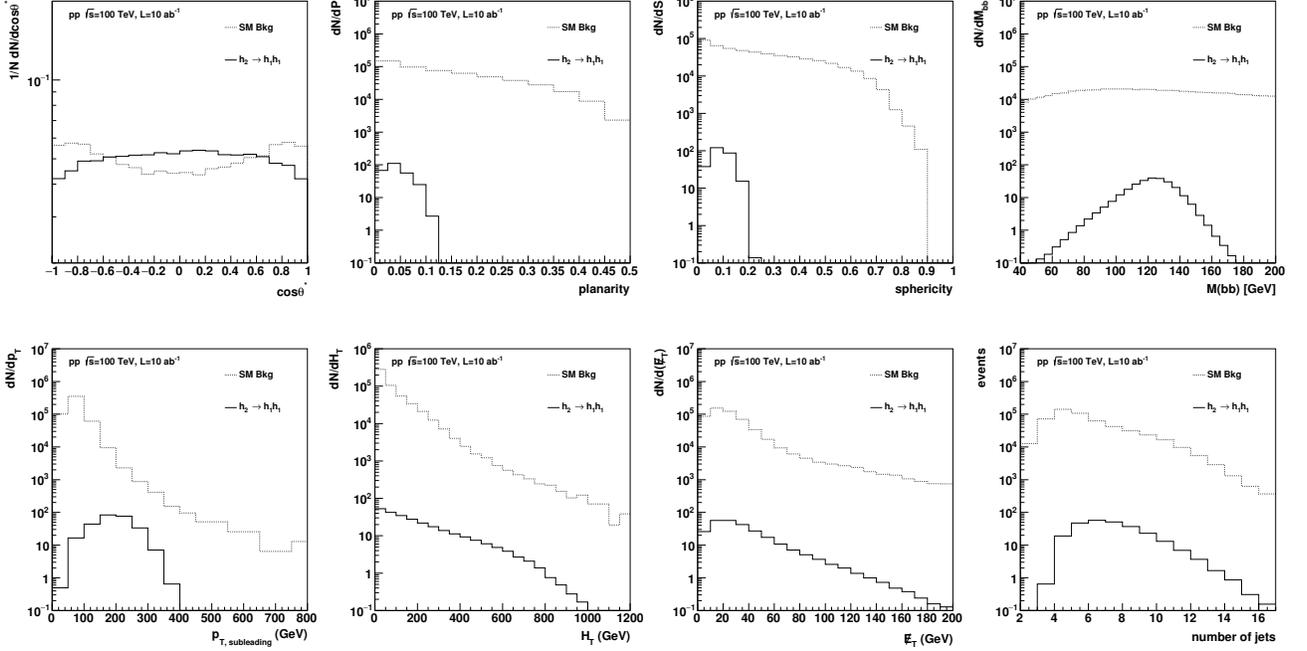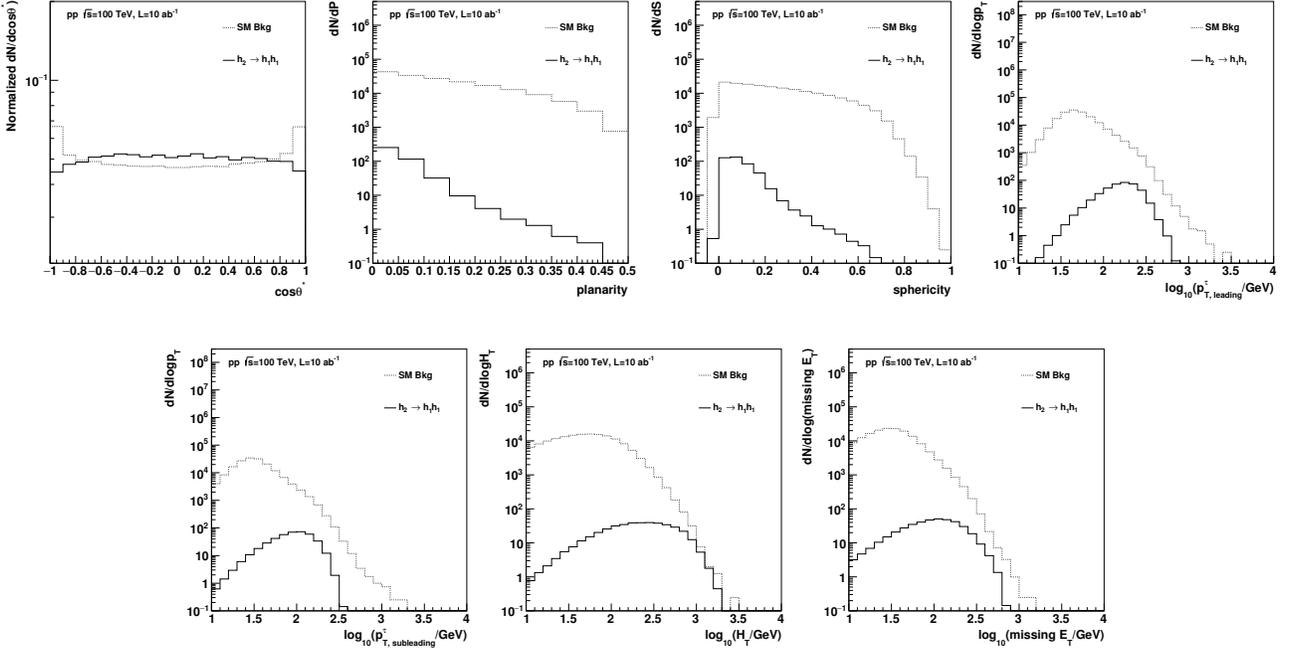

FIG. 8: Additional kinematics distributions for 4τ final state, used as inputs to the BDT. The signal distributions correspond to BM10$^{\mathrm{max}}$.

TABLE VI: Cross sections and BDT analysis results for the 4τ final state, for benchmark points yielding the maximum signal cross section.

	14 TeV		50 TeV		100 TeV				200 TeV	
		3 ab^{-1}		30 ab^{-1}		3 ab^{-1}	10 ab^{-1}	30 ab^{-1}		30 ab^{-1}
	σ_{XS}(ab)	N_σ	σ_{XS}(ab)	N_σ	σ_{XS}(ab)	N_σ	N_σ	N_σ	σ_{XS}(ab)	N_σ
Background	7,500		30,000		55,000				118,000	
B1	457	14.1	5,440	216	16,400	136	248	430	44,000	754
B2	368	12.1	4,480	191	13,600	121	221	383	36,800	668
B3	126	5.5	1,710	96.8	5,400	64.0	117	202	15,100	369
B4	82.9	4.1	1,200	76.2	3,890	51.8	94.6	164	11,100	302
B5	35.2	2.1	558	43.1	1,860	30.1	54.9	95.2	5,400	179
B6	19.7	1.3	338	29.3	1,160	20.7	37.8	65.5	3,400	128
B7	13.1	0.92	238	22.9	836	16.4	30.0	52.0	2,500	100
B8	7.0	0.57	138	14.6	497	11.0	20.2	34.9	1,540	69.0
B9	3.0	0.26	62.8	7.3	232	5.6	10.2	17.7	731	35.6
B10	1.5	0.15	35.1	4.4	133	3.4	6.2	10.7	426	22.9
B11	0.41	0.04	10.3	1.4	40.3	1.1	2.0	3.5	132	7.7

TABLE VII: Cross sections and BDT analysis results for the 4τ final state, for benchmark points yielding the minimum signal cross section.

	14 TeV		50 TeV		100 TeV				200 TeV	
		3 ab^{-1}		30 ab^{-1}		3 ab^{-1}	10 ab^{-1}	30 ab^{-1}		30 ab^{-1}
	σ_{XS} (ab)	N_σ	σ_{XS} (ab)	N_σ	σ_{XS} (ab)	N_σ	N_σ	N_σ	σ_{XS} (ab)	N_σ
Background	7,500		30,000		55,000				118,000	
B1	8.1	0.33	96.7	6.0	291	4.1	7.5	12.9	784	23.5
B2	10.1	0.46	122	7.7	371	5.3	9.5	16.5	1,003	30.4
B3	7.9	0.41	108	7.8	341	5.5	10.0	17.4	953	33.1
B4	3.4	0.19	49.9	4.1	162	3.0	5.4	9.3	463	18.1
B5	3.2	0.21	53.6	5.1	183	3.7	6.8	11.8	540	23.4
B6	4.1	0.27	71.2	6.8	245	5.1	9.3	16.1	728	32.7
B7	2.5	0.18	45.3	4.7	159	3.6	6.5	11.3	483	22.6
B8	1.4	0.12	29.0	3.1	105	2.4	4.4	7.7	238	16.6
B9	0.87	0.08	18.9	2.3	70.3	1.8	3.2	5.6	223	11.7
B10	0.86	0.08	20.2	2.6	77.2	2.0	3.7	6.4	250	14.1
B11	0.32	0.03	8.1	1.1	31.5	0.90	1.6	2.8	103	6.0

Decay channel	Branching ratio	Uncertainty
$b\bar{b}b\bar{b}$	$3.33 \cdot 10^{-1}$	$\pm\, 2.20 \cdot 10^{-2}$
$\tau\tau b\bar{b}$	$7.29 \cdot 10^{-2}$	$\pm\, 4.80 \cdot 10^{-3}$
$W^+(\to l\nu)W^-(\to l\nu)b\bar{b}$	$1.09 \cdot 10^{-2}$	$\pm\, 5.93 \cdot 10^{-4}$
$\tau\tau\tau\tau$	$3.99 \cdot 10^{-3}$	$\pm\, 4.55 \cdot 10^{-4}$
$\gamma\gamma b\bar{b}$	$2.63 \cdot 10^{-3}$	$\pm\, 1.58 \cdot 10^{-4}$
$W^+(\to l\nu)W^-(\to l\nu)\tau\tau$	$1.20 \cdot 10^{-3}$	$\pm\, 8.56 \cdot 10^{-5}$
$\gamma\gamma\tau\tau$	$2.88 \cdot 10^{-4}$	$\pm\, 2.19 \cdot 10^{-5}$
$b\bar{b}\mu^+\mu^-$	$2.53 \cdot 10^{-4}$	$\pm\, 1.73 \cdot 10^{-5}$
$Z(\to l^+l^-)Z(\to l^+l^-)b\bar{b}$	$1.41 \cdot 10^{-4}$	$\pm\, 7.64 \cdot 10^{-6}$
$b\bar{b}Z(\to l^+l^-)\gamma$	$1.21 \cdot 10^{-4}$	$\pm\, 1.16 \cdot 10^{-5}$
$W^+(\to l\nu)W^-(\to l\nu)W^+(\to l\nu)W^-(\to l\nu)$	$8.99 \cdot 10^{-5}$	$\pm\, 7.73 \cdot 10^{-6}$
$\gamma\gamma W^+(\to l\nu)W^-(\to l\nu)$	$4.32 \cdot 10^{-5}$	$\pm\, 2.85 \cdot 10^{-6}$
$\tau\tau\mu^+\mu^-$	$2.77 \cdot 10^{-5}$	$\pm\, 2.29 \cdot 10^{-6}$
$Z(\to l^+l^-)Z(\to l^+l^-)\tau\tau$	$1.54 \cdot 10^{-5}$	$\pm\, 1.10 \cdot 10^{-6}$
$\tau\tau Z(\to l^+l^-)\gamma$	$1.32 \cdot 10^{-5}$	$\pm\, 1.41 \cdot 10^{-6}$
$\gamma\gamma\gamma\gamma$	$5.20 \cdot 10^{-6}$	$\pm\, 5.20 \cdot 10^{-7}$
$W^+(\to l\nu)W^-(\to l\nu)\mu^+\mu^-$	$4.15 \cdot 10^{-6}$	$\pm\, 3.07 \cdot 10^{-7}$
$Z(\to l^+l^-)Z(\to l^+l^-)W^+(\to l\nu)W^-(\to l\nu)$	$2.31 \cdot 10^{-6}$	$\pm\, 1.41 \cdot 10^{-7}$
$W^+(\to l\nu)W^-(\to l\nu)Z(\to l^+l^-)\gamma$	$1.99 \cdot 10^{-6}$	$\pm\, 1.98 \cdot 10^{-7}$
$\gamma\gamma\mu^+\mu^-$	$9.99 \cdot 10^{-7}$	$\pm\, 7.80 \cdot 10^{-8}$
$\gamma\gamma Z(\to l^+l^-)Z(\to l^+l^-)$	$5.57 \cdot 10^{-7}$	$\pm\, 3.67 \cdot 10^{-8}$
$\gamma\gamma Z(\to l^+l^-)\gamma$	$4.78 \cdot 10^{-7}$	$\pm\, 4.92 \cdot 10^{-8}$
$Z(\to l^+l^-)Z(\to l^+l^-)\mu^+\mu^-$	$5.35 \cdot 10^{-8}$	$\pm\, 3.95 \cdot 10^{-9}$
$Z(\to l^+l^-)\gamma\mu^+\mu^-$	$4.59 \cdot 10^{-8}$	$\pm\, 4.96 \cdot 10^{-9}$
$Z(\to l^+l^-)Z(\to l^+l^-)Z(\to l^+l^-)\gamma$	$2.56 \cdot 10^{-8}$	$\pm\, 2.55 \cdot 10^{-9}$
$Z(\to l^+l^-)Z(\to l^+l^-)Z(\to l^+l^-)Z(\to l^+l^-)$	$1.49 \cdot 10^{-8}$	$\pm\, 1.28 \cdot 10^{-9}$
$Z(\to l^+l^-)\gamma Z(\to l^+l^-)\gamma$	$1.10 \cdot 10^{-8}$	$\pm\, 1.97 \cdot 10^{-9}$

TABLE VIII: Branching ratios for final states arising from double-Higgs production, with the requirement of leptonic decays of W and Z bosons.

[1] ATLAS, G. Aad *et al.*, Phys.Lett. **B716**, 1 (2012), 1207.7214.

[2] CMS, S. Chatrchyan *et al.*, Phys.Lett. **B716**, 30 (2012), 1207.7235.

[3] Planck, P. A. R. Ade *et al.*, Astron. Astrophys. **571**, A16 (2014), 1303.5076.

[4] A. Sakharov, Pisma Zh.Eksp.Teor.Fiz. **5**, 32 (1967).

[5] D. E. Morrissey and M. J. Ramsey-Musolf, New J. Phys. **14**, 125003 (2012), 1206.2942.

[6] Y. Aoki, F. Csikor, Z. Fodor, and A. Ukawa, Phys. Rev. **D60**, 013001 (1999), hep-lat/9901021.

[7] F. Csikor, Z. Fodor, and J. Heitger, Phys. Rev. Lett. **82**, 21 (1999), hep-ph/9809291.

[8] M. Laine and K. Rummukainen, Nucl. Phys. Proc. Suppl. **73**, 180 (1999), hep-lat/9809045.

[9] M. Gurtler, E.-M. Ilgenfritz, and A. Schiller, Phys. Rev. **D56**, 3888 (1997), hep-lat/9704013.

[10] K. Kajantie, M. Laine, K. Rummukainen, and M. E. Shaposhnikov, Phys. Rev. Lett. **77**, 2887 (1996), hep-ph/9605288.

[11] S. Profumo, M. J. Ramsey-Musolf, and G. Shaughnessy, JHEP **08**, 010 (2007), 0705.2425.

[12] A. Noble and M. Perelstein, Phys. Rev. **D78**, 063518 (2008), 0711.3018.

[13] D. Curtin, P. Meade, and C.-T. Yu, JHEP **11**, 127 (2014), 1409.0005.

[14] J. R. Espinosa, T. Konstandin, and F. Riva, Nucl. Phys. **B854**, 592 (2012), 1107.5441.

[15] J. M. No and M. Ramsey-Musolf, Phys. Rev. **D89**, 095031 (2014), 1310.6035.

[16] S. Profumo, M. J. Ramsey-Musolf, C. L. Wainwright, and P. Winslow, Phys. Rev. **D91**, 035018 (2015), 1407.5342.

[17] M. Maniatis, Int. J. Mod. Phys. **A25**, 3505 (2010), 0906.0777.

[18] U. Ellwanger, C. Hugonie, and A. M. Teixeira, Phys. Rept. **496**, 1 (2010), 0910.1785.

[19] D. O'Connell, M. J. Ramsey-Musolf, and M. B. Wise, Phys. Rev. **D75**, 037701 (2007), hep-ph/0611014.

[20] V. Barger, P. Langacker, M. McCaskey, M. J. Ramsey-Musolf, and G. Shaughnessy, Phys. Rev. **D77**, 035005 (2008), 0706.4311.

[21] X.-G. He and J. Tandean, Phys. Rev. **D88**, 013020 (2013), 1304.6058.

[22] J. M. Cline, K. Kainulainen, P. Scott, and C. Weniger, Phys. Rev. **D88**, 055025 (2013), 1306.4710, [Erratum: Phys. Rev.D92,no.3,039906(2015)].

[23] Y. Mambrini, Phys. Rev. **D84**, 115017 (2011), 1108.0671.

[24] M. Gonderinger, Y. Li, H. Patel, and M. J. Ramsey-Musolf, JHEP **01**, 053 (2010), 0910.3167.

[25] J. R. Espinosa, T. Konstandin, J. M. No, and M. Quiros, Phys. Rev. **D78**, 123528 (2008), 0809.3215.

[26] C. P. Burgess, M. Pospelov, and T. ter Veldhuis, Nucl. Phys. **B619**, 709 (2001), hep-ph/0011335.

[27] J. McDonald, Phys. Rev. **D50**, 3637 (1994), hep-ph/0702143.

[28] M. Gorbahn, J. M. No, and V. Sanz, JHEP **10**, 036 (2015), 1502.07352.

[29] M. Baak *et al.*, Eur. Phys. J. **C72**, 2205 (2012), 1209.2716.

[30] ATLAS, G. Aad *et al.*, Eur. Phys. J. **C76**, 45 (2016), 1507.05930.

[31] ATLAS, G. Aad *et al.*, Phys. Lett. **B755**, 285 (2016), 1512.05099.

[32] CMS, S. Chatrchyan *et al.*, Eur. Phys. J. **C73**, 2469 (2013), 1304.0213.

[33] CMS, V. Khachatryan *et al.*, JHEP **10**, 144 (2015), 1504.00936.

[34] LHC Higgs Cross Section Working Group, J. R. Andersen *et al.*, (2013), 1307.1347.

[35] H. H. Patel and M. J. Ramsey-Musolf, JHEP **07**, 029 (2011), 1101.4665.

[36] M. Pietroni, Nucl. Phys. **B402**, 27 (1993), hep-ph/9207227.

[37] C. L. Wainwright, Comput. Phys. Commun. **183**, 2006 (2012), 1109.4189.

[38] A. Djouadi, Phys. Rept. **457**, 1 (2008), hep-ph/0503172.

[39] A. V. Kotwal, S. Chekanov, and M. Low, Phys. Rev. **D91**, 114018 (2015), 1504.08042.

[40] D. Buttazzo, F. Sala, and A. Tesi, JHEP **11**, 158 (2015), 1505.05488.

[41] J. Alwall *et al.*, JHEP **07**, 079 (2014), 1405.0301.

[42] T. Sjostrand, S. Mrenna, and P. Z. Skands, JHEP **05**, 026 (2006), hep-ph/0603175.

[43] T. Sjostrand, S. Mrenna, and P. Z. Skands, Comput. Phys. Commun. **178**, 852 (2008), 0710.3820.

[44] A. D. Martin, W. J. Stirling, R. S. Thorne, and G. Watt, Eur. Phys. J. **C63**, 189 (2009), 0901.0002.

[45] S. V. Chekanov, K. Strand, and P. Van Gemmeren, Comput. Phys. Commun. **185**, 2629 (2014), 1311.1229.

[46] S. V. Chekanov, Next generation input-output data format for HEP using Google's protocol buffers, in *Community Summer Study 2013: Snowmass on the Mississippi (CSS2013) Minneapolis, MN, USA, July 29-August 6, 2013*, 2013, 1306.6675.

[47] R. Brun and F. Rademakers, Nuclear Instruments and Methods in Physics Research Section A: Accelerators, Spectrometers, Detectors and Associated Equipment **389**, 81 (1997), New Computing Techniques in Physics Research V.

[48] M. Cacciari, G. P. Salam, and G. Soyez, JHEP **04**, 063 (2008), 0802.1189.

[49] M. Cacciari, G. P. Salam, and G. Soyez, Eur. Phys. J. **C72**, 1896 (2012), 1111.6097.

[50] H.-J. He, J. Ren, and W. Yao, Phys. Rev. **D93**, 015003 (2016), 1506.03302.

[51] A. Azatov, R. Contino, G. Panico, and M. Son, Phys. Rev. **D92**, 035001 (2015), 1502.00539.

[52] CMS, V. Khachatryan *et al.*, Journal of Instrumentation **10**, P08010 (2015).

[53] ATLAS, G. Aad *et al.*, JHEP **08**, 148 (2015), 1505.07018.

[54] ATLAS, G. Aad *et al.*, JINST **11**, P04008 (2016), 1512.01094.

[55] CMS, S. Chatrchyan *et al.*, Journal of Instrumentation **8**, P04013 (2013).

[56] ATLAS, G. Aad *et al.*, JINST **3**, S08003 (2008).

[57] CMS, S. Chatrchyan *et al.*, JINST **3**, S08004 (2008).

[58] ATLAS, G. Aad *et al.*, Eur. Phys. J. **C74**, 3071 (2014), 1407.5063.

[59] CMS, S. Chatrchyan *et al.*, Journal of Instrumentation **6**, P11002 (2011).

[60] ATLAS, G. Aad *et al.*, Eur. Phys. J. **C73**, 2306 (2013), 1210.6210.

[61] ATLAS, G. Aad *et al.*, Eur. Phys. J. **C72**, 2211 (2012), 1206.2135.

[62] V. A. Okorokov, Int. J. Mod. Phys. **A27**, 1250037 (2012), 1105.4784.

[63] ATLAS, G. Aad *et al.*, Eur. Phys. J. **C75**, 303 (2015), 1412.7086.

[64] ATLAS, G. Aad *et al.*, JHEP **07**, 157 (2015), 1502.07177.

[65] ATLAS, G. Aad *et al.*, Eur. Phys. J. **C75**, 69 (2015), 1409.6190.